ARF6 is a host factor for SARS-CoV-2 infection *in vitro*.

C. Mirabelli[1#], E.J. Sherman[2#], J. Bragazzi Cunha[2], J.W. Wotring[3], J. El Saghir[4], J. Harder[4], M. Kretzler[4], J.Z. Sexton[3], B.T. Emmer[2] and C.E. Wobus[1*]*

[1]Department of Microbiology and Immunology, University of Michigan medical school, Ann Arbor (MI, USA
[2] Department of Internal Medicine, Division of Hospital Medicine, University of Michigan, Ann Arbor (MI), USA
[3] Department of Internal Medicine, Division of Gastroenterology and Hepatology, University of Michigan, Ann Arbor, Michigan, USA
[4]Department of Internal Medicine, Division of Nephrology, University of Michigan, Ann Arbor, Michigan, USA

[#]Current affiliation:

C. Mirabelli, *Institut für Virologie und Zellbiologie, University of Lübeck, Germany*
E.J. Sherman, *Territory Manager at Takara Bio USA, Inc. - MI, MN, IN, KY*

[*]Corresponding authors: camirabe@med.umich.edu, cwobus@umich.edu

Abstract

SARS-CoV-2 is a newly emerged beta-coronavirus that enter cells via two routes, direct fusion at the plasma membrane or endocytosis followed by fusion with the late endosome/lysosome. While the viral receptor, ACE2, multiple entry factors, and the mechanism of fusion of the virus at the plasma membrane have been extensively investigated, viral entry via the endocytic pathway is less understood. By using a human hepatocarcinoma cell line, Huh-7, which is resistant to the antiviral action of the TMPRSS2 inhibitor camostat, we discovered that SARS-CoV-2 entry is not dependent on dynamin but dependent on cholesterol. ADP-ribosylation factor 6 (ARF6) has been described as a host factor for SARS-CoV-2 replication and it is involved in the entry and infection of several pathogenic viruses. Using CRISPR-Cas9 genetic deletion, we observed that ARF6 is important for SARS-CoV-2 uptake and infection in Huh-7. This finding was corroborated using a pharmacologic inhibitor, whereby the ARF6 inhibitor NAV-2729 showed a dose-dependent inhibition of viral infection. Importantly, NAV-2729 reduced SARS-

CoV-2 viral loads also in more physiologic models of infection: Calu-3 and kidney organoids. This highlighted the importance of ARF6 in multiple cell contexts. Together, these experiments points to ARF6 as a putative target to develop antiviral strategies against SARS-CoV-2.

Keywords: SARS-CoV-2, entry, ARF6, endocytic pathway, therapeutic targets

40 **Introduction**

41 SARS-CoV-2 is a newly emerged beta-coronavirus and causative agent of the COVID-19
42 pandemic. While several vaccines and antivirals have been approved to limit severe COVID-19,
43 the spread of the virus is not yet under control. This highlights the importance of developing
44 additional therapeutic strategies that can complement vaccine rollout, especially at the epidemic
45 centers. Given the propensity of RNA viruses to develop drug resistance, there is an unmet need
46 for additional antiviral compounds that can curb the infection and transmission by targeting
47 additional steps in the virus life cycle. Viral entry is a step in the viral cycle that is promising for
48 antiviral development. This important step of the viral life cycle has been characterized very
49 early after the isolation of SARS-CoV-2, leading to the discovery of the uncoating receptor,
50 ACE2 [1] and the two entry pathways [2]: via plasma membrane fusion or endocytosis.
51 Membrane fusion at the plasma membrane occurs after SARS-CoV-2 surface (S) protein
52 activation by proteinase cleavage, including TMPRRS2, whereas fusion in the endocytic
53 compartment requires the intracellular protease cathepsin L. The pathway and molecular players
54 that govern endocytosis-mediated entry are however poorly characterized. Endocytosis of viruses
55 can occur via different pathways, including clathrin-mediated endocytosis (CME), caveolar or
56 lipid raft-mediated endocytosis, macropinocytosis and variations of these themes [3]. Some
57 viruses are able to use more than one pathway, which introduces a further level of ambiguity to
58 the classification of virus entry pathways. Research on SARS-CoV-2 endocytic-mediated entry
59 has been scant. A single report using a lentivirus system in ACE-2 overexpressing 293T cells
60 suggests that SARS-CoV-2 endocytosis is dependent on clathrin and dynamin [4]. However,
61 studies on SARS-CoV-2 endocytic entry pathway in the context of a productive infection were
62 missing at the beginning of our investigation.

63 ADP-ribosylation factor 6 (ARF6) is a multi-functional cellular protein. It directly activates lipid
64 modifying enzymes, such as phosphatidylinositol 4-phosphate 5-kinase, and it stimulates actin
65 polymerization. ARF6-positive cargoes can be directly transported on microtubule filaments; and
66 it also assists autophagy, particularly the initiation and autophagosome formation [5]. Because of
67 its roles in endocytosis and trafficking, ARF6 is co-opted by several pathogens; bacteria (e.g.,
68 enteropathogenic and enterohemorrhagic *Escherichia coli*, *Salmonella Typhimurium, Shigella*)
69 and viruses (e.g., HIV-1, Coxsackievirus A and B, Epstein Barr virus). ARF6 was recently
70 identified as a cellular interaction partner of the uridine-specific endoribonuclease Nsp15 of
71 SARS-CoV-2 [6] and a recent re-analysis of a RNA sequencing dataset of infected A549-ACE2
72 cells, ARF6 is involved in three of the four identified modules mediating host cell responses
73 during SARS-CoV-2 infection, i.e., viral entry, regulation and signaling, and immune responses
74 [7]. We therefore sought out to determine the role of ARF6 in SARS-CoV-2 endocytosis and,
75 more broadly, infection.
76 We first found that in the human hepatocarcinoma cell line, Huh-7 SARS-CoV-2 is resistant to
77 camostat, a specific TMPRSS2 inhibitor, and hence SARS-CoV-2 entry mostly relies on
78 endocytosis for infection. By genetic depletion and pharmacologic inhibition, we further
79 demonstrated that SARS-CoV-2 entry into Huh-7 is dynamin-independent but dependent on
80 cholesterol and ARF6. This host factor is also important for infection in the more physiologic
81 relevant models of human lung Calu3 cells and kidney organoids, suggesting that ARF6 might
82 be an effective therapeutic target.
83
84 **Material and Methods**

85 **Cells and virus.** Human hepatocarcinoma cells, Huh-7, and human lung adenocarcinoma cells,
86 and Calu3, were obtained by collaborators and maintained at 37 °C and 5% CO2 in Dulbecco's
87 modified Eagle's medium (DMEM) (Gibco), supplemented with 10% heat-inactivated fetal
88 bovine serum (FBS), Hepes, nonessential amino acids, L-glutamine, and 1× Pen-Strep (Gibco).
89 Kidney organoids were generated using human embryonic stem cells (UM77-2), as previously
90 described [8]. SARS-CoV-2 was obtained through BEI Resources (SARS-Related Coronavirus
91 2, Isolate USA-WA1/2020, NR-52281 and Isolate hCoV-19/USA/GA-EHC-2811C/2021
92 [Omicron Variant] NR-56481). Lack of genetic drift of our viral stock was confirmed by deep
93 sequencing. Viral titers were determined by $TCID_{50}$ assays in Vero E6 cells (Reed and Muench
94 method). All experiments using SARS-CoV-2 were performed at the University of Michigan
95 under Biosafety Level 3 (BSL3) protocols in compliance with containment procedures in
96 laboratories approved for use by the University of Michigan Institutional Biosafety Committee
97 and Environment, Health and Safety.
98
99 **SARS-CoV-2 infection and quantification by immunofluorescence.** Cells were seeded at
100 3,000 cells/well (384-well plate, Perkin-Elmer, 6057300) or 10,000 cells/well (96-well plates,
101 Costar, 3916) and allowed to adhere overnight. Compounds were then added to the cells and
102 incubated for 2 hrs at 37 °C. Plates were then transferred to BSL3 containment and infected with
103 SARS-CoV-2 WA1 or Omicron at a MOI of 1. In the case of infection with the Omicron variant,
104 a pre-treatment of the virus with 10 μM of porcine trypsin (Millipore-Sigma, cat nr. T0303-1G)
105 for 15 min at 37'C was included. After 1 h of absorption on cell (final concentration of trypsin
106 was 2 μM), the virus inoculum was removed and fresh media with inhibitors was added.
107 Uninfected and vehicle-treated infected cells were included as negative and positive controls,

108 respectively. Plates were then stained as previously described [9] by using anti-nucleocapsid
109 protein (anti-N) SARS-CoV-2 antibody (Antibodies Online; catalog no. ABIN6952432)
110 followed by staining with secondary antibody Alexa-647 (goat anti-mouse; Thermo Fisher;
111 A21235) and DAPI for nuclei staining. Stained cells were acquired on Thermo Fisher CX5 high-
112 content microscopes with a 20×/0.45 N.A. LUCPlan FLN objective. Laser autofocus was
113 performed and 9 or 18 fields per well were imaged covering ~80% of the well area. Images were
114 analyzed with Cell Profiler software and percent of infected cells (N-positive) was calculated on
115 the total cell count (i.e., DAPI positive).
116
117 **SARS-CoV-2 infection and quantification by $TCID_{50}$ assay.** 200,000 Huh-7 or Huh-7 knock-
118 out (KO) cells were seeded in 12-well plates. For the Calu-3, 100,000 cells were seeded in 24-
119 well plates. The next day or at 80% cell confluency, compounds were added to the cells and
120 incubated for 2 hrs. Cells were then infected with SARS-CoV-2 WA1 at a MOI of 1 for 1 h at 37
121 °C. Inoculum was removed, cells were washed 3 times with PBS without Magnesium and
122 Calcium (PBS-/-) and fresh medium was added. Cells were harvested 1 day post infection (dpi)
123 and lysates were obtained by one cycle of freeze-thaw. For the kidney organoids, 3D-spheres
124 were collected in 1.5 mL tubes and infected with SARS-CoV-2 at an estimated MOI of 1. After
125 infection, 3D-spheroids were washed 3 times with PBS-/- and gentle centrifugation (80 g for 2
126 min). A minimum of four 3D-spheroids were transferred in a 96-well plate and medium with
127 selected compounds was added to the cells. SARS-CoV-2 infection was quantified by $TCID_{50}$ on
128 pre-seeded Vero E6 cells (Reed and Muench method) or by RT-qPCR (IDT technologies,
129 Charité kit) after RNA extraction with TRI reagent and Direct-Zol RNA miniprep kit (Zymo
130 Research).

131

132 **Generation of CRISPR-KO cell lines.** Individual guide RNA (gRNA) sequences
133 (**Supplemental Table 1**) were cloned into BsmBI-digested lentiCRISPRv2 (Addgene #52961, a
134 gift from Feng Zhang [10]) and resulting lentiviral stocks prepared as previously described [11].
135 Huh-7 and Calu-3 cells were transduced with lentiviral stocks at an MOI of ~1, treated 1 day
136 later with puromycin (3 ug/mL) until death of control uninfected cells was complete, and
137 passaged as needed to maintain logarithmic phase growth for 2-3 weeks. Cells were then either
138 harvested for mRNA and protein preparations or infected with SARS-CoV-2 infection as
139 described above.

140

141 **Attachment/internalization assay.** Huh-7 or ARF6-KO cells were plated in 48-well plates at
142 100,000 cells per well and allowed to adhere overnight. The following day, NAV-2729 was
143 added at the indicated concentration and incubated for 2 hrs. Following compound incubation,
144 cells were infected with SARS-CoV-2 at an MOI of 10 for 1 h at 4 °C to allow for viral binding.
145 Cells were then washed three times with ice-cold PBS-/- to remove unbound virus and harvested
146 in TRI reagent. Another set of treated-infected cells was transferred at 37°C to allow for viral
147 internalization. One hour after incubation, cells were treated with trypsin to remove bound-not
148 internalized virus and after centrifugation at 500 x g for 5 min, cells were harvested in TRI
149 reagent. RNA was extracted by using the Direct-Zol RNA miniprep kit (Zymogen; R2052) and
150 viral RNA was quantified by RT-qPCR. Proportion of internalized virus was calculated over the
151 bound virus.

152

153 **Results**

154 **SARS-CoV-2 infection in Huh-7 is resistant to camostat treatment but sensitive to Z-FA-**
155 **FMK.**
156 To investigate SARS-CoV-2 endocytosis, we screened a range of cell lines for the antiviral
157 activity of camostat mesylate, a specific inhibitor of TMPRSS2 (data not shown). Infection
158 readout was carried out with an imaging-based pipeline by using a SARS-CoV-2 anti-
159 nucleocapsid (N) antibody to detect infected cells. Interestingly, in the human hepatocarcinoma
160 cell line Huh-7, SARS-CoV-2 was completely resistant to the antiviral action of camostat
161 (**Figure 1A**). In contrast, treatment with the irreversible cysteine protease inhibitor Z-FA-FMK,
162 an inhibitor of the intracellular protease cathepsin L, resulted in a strong antiviral activity with
163 EC_{50} of 11 nM (**Figure 1B**) [9]. Representative images of SARS-CoV-2-infected Huh-7 in the
164 presence of Z-FA-FMK and camostat are available in **Figure 1C**. These data suggest that SARS-
165 CoV-2 entry into Huh-7 cells is likely mediated by endocytosis and not fusion at the plasma
166 membrane. Therefore, Huh-7 cells represent a model cell line to mechanistically study SARS-
167 CoV-2 endocytic entry.
168
169 **SARS-CoV-2 uptake into Huh-7 cells is dynamin-independent**
170 A previous report with a lentivirus system in ACE-2 overexpressing 293T cells, suggests that
171 SARS-CoV-2 endocytosis is dependent on clathrin and dynamin [4]. We therefore determined if
172 dynamin governs SARS-CoV-2 entry into Huh-7 cells by using dynasore, a specific GTPase
173 inhibitor of dynamin I, II and Drp1 (the mitochondrial dynamin) [12]. ß-methyl cyclodextrin, a
174 cholesterol-removing agent that mostly blocks formation of lipid rafts important for endocytosis,
175 was used as a positive control since ACE2 is present in lipid rafts [13] and SARS-CoV entry is
176 dependent on cholesterol [14]. Huh-7 cells were pretreated 2 hrs prior to infection with selected

177 compounds at non-toxic concentrations (**Supplementary Figure 1**) and infection with SARS-
178 CoV-2 was quantified by N protein expression. As expected, treatment with ß-methyl
179 cyclodextrin blocked viral infection. However, in contrast with previous findings, treatment with
180 the specific dynamin inhibitor dynasore, revealed a significant increase in the percentage of
181 infected cells (**Figure 2)**. This observation points to a dynamin-independent but cholesterol-
182 dependent endocytic uptake mechanism of SARS-CoV-2 into Huh-7 cells.
183
184 **Genetic perturbation of ARF6 results in a reduction in the percentage of infected cells.**
185 Dynamin-independent pathways are governed by the Rho GTPase-activating protein 26 (GRAF-
186 1), flotillin (FLOT-1) or ADP-ribosylation factor 6 (ARF6) [15]. Since ARF6 was recently
187 described for mediating host cell responses during SARS-CoV-2 infection, we generated two
188 polyclonal populations of CRISPR-targeted cells with gRNAs specific for ARF6 (clones 1 and
189 2). ARF6 depletion was confirmed by RT-qPCR, whereby the efficacy of knock-out (KO) was
190 measured as a percentage of mRNA target gene expression compared to the non-targeting guide
191 (NTg) Huh-7 cell line (for clone 1, c1=39% and clone 2, c2=56%) and by Western blot
192 (**Supplementary Figure 2A**). To test the efficacy of the CRISPR pipeline, an ACE2-KO Huh-7
193 line was generated in parallel as a control. Cells were infected with SARS-CoV-2 at MOI of 1
194 and harvested 1 and 2 dpi. A combination of $TCID_{50}$ assay and RT-qPCR were used to quantify
195 viral infection and replication, respectively (**Figure 3A and 3B**). No significant differences were
196 detected by $TCID_{50}$ between ARF6 KO and NTg cells whereas replication was ablated in the
197 control ACE2-KO Huh-7 cells. To independently validate these findings, an imaging-based
198 readout for SARS-CoV-2 infection was used, since it enables analysis at the single cell level.
199 The assay was also adjusted to a 1 dpi readout and infecting cells with SARS-CoV-2 at the

200 higher MOI of 10. For ease of experimentation, only ARF6-KO c1, with lower expression of the
201 target gene was used for this analysis. Representative images at 1 dpi are shown in **Figure 3C**.
202 Intriguingly, we observed a significant decrease in the percentage of infected cells in ARF6 KO
203 than the NTg cells, suggesting that ARF6 might be involved in SARS-CoV-2 entry (**Figure 3C**).
204 Collectively, these data suggest a role for ARF6 in SARS-CoV-2 infection in Huh-7.
205
206 **Pharmacologic inhibition of ARF6 blocks SARS-CoV-2 internalization**
207 ARF6 has been the object of extensive studies and specific small molecule inhibitors are
208 available commercially. We therefore selected the inhibitor NAV-2729 to test its effect on
209 SARS-CoV-2 infection. Huh-7 cells were pre-treated with a 1:2 dilution series of compounds
210 and infected with SARS-CoV-2 at MOI of 1. NAV-2729 showed a dose-dependent inhibition of
211 infection (**Figure 4A**), suggesting that ARF6 is an important factor for SARS-CoV-2 infection in
212 Huh-7. We next selected an efficacious non-toxic concentration of NAV-2729 (**Supplementary**
213 **figure 1A**) to confirm inhibition by $TCID_{50}$ (**Figure 4B**). Treatment with NAV-2729 resulted in
214 a ~2.5-Log reduction in viral infection in the NTg control. We also wanted to assess whether
215 viral entry into ARF6-KO switched to a dynamin-dependent entry mechanisms but treatment of
216 the ARF6-KO cells with dynasore did not result in changes to infection, further corroborating
217 that dynamin is not involved in SARS-CoV-2 endocytosis in Huh-7 (**Figure 4B**). To determine
218 whether the NAV-2729 inhibitor worked at the level of viral internalization, an
219 attachment/internalization assay was performed. Briefly, NTg cells were pre-treated with NAV-
220 2729 and infected with SARS-CoV-2 at the MOI of 10. ARF6-KO cells were included as a
221 control. One hour post-inoculation on ice, cells were washed and one set was harvested to
222 quantify the virus attached at the cell surface by RT-qPCR. While treatment with NAV-2729 did

223 not affect virus binding to NTg cells, ARF6-KO cells showed a significantly higher level of
224 SARS-CoV-2 binding compared to NTg cells (**Figure 4C**). The other batch was incubated at
225 37ºC for 1 hr to allow for viral internalization, and after bound-not internalized virus was
226 removed by a treatment with trypsin, cells were harvested to quantify the internalized virus by
227 RT-qPCR. To control for differences in SARS-CoV-2 binding between cells, we calculated the
228 ratio of internalized *versus* bound virus (**Figure 4D**). NAV-2729 reduced viral internalization by
229 75% *versus* the more modest 25% observed in the ARF6-KO, suggesting that ARF6 is a factor
230 that governs endocytosis in Huh-7.
231
232 **ARF6 is an important host factor for SARS-CoV-2 infection in more physiological relevant**
233 **infection models**
234 To test the importance of ARF6 in other cellular contexts, we used the ARF6 inhibitor NAV-
235 2729 in more physiologic relevant models that are sensitive to camostat: human renal organoids
236 and human lung Calu-3 cells [16]. In both models, treatment with non-toxic concentration of
237 NAV-2729 (**Supplementary figure 1B**) resulted in a significant reduction of viral replication
238 (**Figure 5A and 5B**). The nucleoside inhibitor remdesivir was used as a control. In addition, we
239 performed CRISPR-Cas9 knockout of ARF6 in Calu-3 cells (**Supplementary figure 2B**) to
240 corroborate the pharmacologic studies with NAV-2729. Infection with SARS-CoV-2 at an MOI
241 of 1 was less efficient in the Calu3 line transduced with the ARF6-targeting guide (ARF6) than
242 in Calu-3 cells transduced with a non-targeting RNA guide (NTg) (**Figure 5B**). Although the
243 data did not reach statistical significance, the decrease in SARS-CoV-2 infection in Calu3 ARF6-
244 KO cells was more pronounced than in Huh-7 ARF6 KO cells (compare **Figure 5B** with **Figure**
245 **3A**), suggesting that ARF6 might play additional roles in Calu-3 cells compared to Huh-7.

246 Lastly, to shed more light on the mechanism by which ARF6 assists SARS-CoV-2 replication in
247 Calu-3 cells, we infected NTg and ARF6 KO Calu-3 cells with SARS-CoV-2 Omicron variant.
248 This variant has been demonstrated to rely primarily on endocytosis and not on membrane fusion
249 for entry *in vitro* and *in vivo* [17]. Both virus isolates were pre-treated with trypsin prior to
250 infection to proteolytically cleave the S protein and bypass the need of cellular proteases [18].
251 Under these conditions, infection of NTg Calu-3 cells with SARS-CoV-2 Omicron resulted in
252 ~15-fold higher infection (as measured by % of N-positive cells at 24 hpt) than with the WA1
253 strain (**Figure 5C**). Infection of ARF6 KO with both strains showed a significant reduction
254 compared to NTg cells, suggesting that ARF6 might play a role in post-entry steps in Calu-3
255 cells. Overall, these results point to the importance of ARF6 in SARS-CoV-2 infection and to a
256 putative therapeutic target against coronavirus infection.
257

258 **Discussion**

259 In this study, we uncovered that ARF6 is a critical player of SARS-CoV-2 infection in cells of
260 liver, lung, and kidney origin. In addition, in Huh7 cells, ARF6 inhibited SARS-CoV-2 uptake
261 with a mechanism that is further dependent on cholesterol but independent of dynamin and by
262 extension likely clathrin-independent. This is consistent with a prior study that excludes the
263 involvement of dynamin, clathrin, caveolin and endophilin A2 for entry of SARS-CoV-2[14] and
264 with the entry pathway identified for SARS-CoV, which is cholesterol-dependent but clathrin-
265 and caveolin-independent [19]. However, our finding differs from a study demonstrating the
266 importance of clathrin in SARS-CoV-2 entry [4]. That study was performed with a lentivirus
267 system in 293T cells and not in the context of authentic SARS-CoV-2 infection. Thus,
268 differences in virus and/or cell type may alter the endocytic uptake pathway. During the revision

269 of this manuscript, Zhou et al. also published that ARF6 is an important host factor for SARS-
270 CoV-2 entry [20]. Specifically, their study used an siRNA approach and SARS-CoV-2
271 pseudovirus to demonstrate a 2-fold reduction of viral entry in Huh-7 cells. This is consistent
272 with the levels of reduction that we observe in the context of SARS-CoV-2 infection in ARF6
273 KO cells (by immunofluorescence) and upon pharmacological inhibition of ARF6 by the specific
274 inhibitor NAV-2729. We posit that the observed effect of ARF6 on infectivity in Huh-7 cells by
275 immunofluorescence but not in infectious virus titers in Figure 3 might be simply due to the
276 tenfold higher MOI used in the former experiment given the heterogeneity of the knockdown.
277 Intriguingly, we observed that CRISPR-depleted cells exhibited a less pronounced phenotype as
278 compared with those treated with the ARF6 specific inhibitor, NAV-2729. This could be due to
279 several reasons. Because of the redundancy of endocytic pathways and lack of an important
280 intracellular trafficking factor, prolonged passaging of the ARF6-KO cells and the potential
281 incomplete activity of the guide RNA as indicated by the qPCR data might have led to
282 compensatory mechanisms and a less uniform phenotype. In contrast, the short-term treatment
283 with a small molecule inhibitor at non-toxic concentrations does not affect or modify the
284 physiology of the cell and reduces the impact of compensatory mechanisms and could thus be
285 more relevant for the study of these redundant endocytic pathways.
286 In our investigation, we expanded on the importance of ARF6 also in the context of infection of
287 other cell types; kidney organoids and Calu3 cells, a model of respiratory epithelial cells. In both
288 systems, the ARF6 inhibitor, NAV-2729, showed a strong antiviral effect. These cell models
289 support SARS-CoV-2 entry also via membrane fusion [21]. ARF6-KO Calu3 or Huh7 cells
290 exhibited a reduction of infection by both immunofluorescence and $TCID_{50}$. These data highlight
291 the important role for ARF6 during SARS-CoV-2 infection. Considering the multiple functions

292 of ARF6 in intracellular membrane trafficking [5] and the observation that the decrease in
293 SARS-CoV-2 infection in Calu3 ARF6-KO cells was more pronounced than in Huh-7 ARF6 KO
294 cells (compare Figure 5B with Figure 3A), we cannot rule out a role for ARF6 in post-entry steps
295 of the viral life cycle. However, additional studies are needed in the future to examine this
296 possibility.
297 It is not known what proportion of SARS-CoV-2 virions is entering via membrane fusion at the
298 plasma membrane or endocytosis *in vivo*. SARS-CoV-2 prefers activation by TMPRSS2 but if
299 the target cells express insufficient TMPRSS2 or if a virus–ACE2 complex does not encounter
300 TMPRSS2, ACE2-bound virus is internalized via endocytosis [2]. TMPRSS2 is found in the
301 gastrointestinal, respiratory, and urogenital epithelium but not in other extra-mucosal
302 compartments (i.e., heart, liver, kidneys, brain, spleen, and lymph nodes), where virus RNA or
303 antigen is found in severe and deadly cases of COVID-19, suggesting that entry and replication
304 of SARS-CoV-2 in these organs might be exclusively driven by endocytosis. It is also possible
305 that SARS-CoV-2 entry occurs by plasma membrane fusion and endocytosis, regardless of the
306 compartment. Therefore, it would be of interest to use NAV-2729 in a small animal model to
307 investigate the *in vivo* relevance of the endocytic pathway and its importance in driving severe
308 disease. Altogether, these data highlight ARF6 as a potential target in the development of
309 therapeutics against COVID-19. Future studies focusing on investigational drugs targeting
310 ARF6, such as Linsitinib that has antiviral activity in a pseudovirus assay [7], could hold
311 promise for the development of additional SARS-CoV-2 therapeutics.
312
313 **Acknowledgement and funding information**

314 We thank Dr. A. Lauring (University of Michigan) for deep sequencing of the viral stock. The
315 work was in part funded by the University of Michigan Biological Science Scholars Program to
316 C.E.W. C.M. was supported by the Marie-Skłodowska-Curie Actions action global fellowship
317 (GA 841247). JZS is supported by the National Institute of Diabetes and Kidney Diseases
318 (R01DK120623) and National Center for Advancing Translational Sciences Grant
319 UL1TR002240. J.W.W. is supported by the Pharmacological Sciences Training Program T32
320 Training Grant GM007767.

321

322 **Conflict of Interest:** The authors declare that there are no conflicts of interest.

323

324 **Reference**

325 1. **Hoffmann M, Kleine-Weber H, Schroeder S, Krüger N, Herrler T, *et al.*** SARS-CoV-
326 2 Cell Entry Depends on ACE2 and TMPRSS2 and Is Blocked by a Clinically Proven
327 Protease Inhibitor. *Cell*. Epub ahead of print 2020. DOI: 10.1016/j.cell.2020.02.052.
328 2. **Jackson CB, Farzan M, Chen B, Choe H**. Mechanisms of SARS-CoV-2 entry into cells.
329 *Nature Reviews Molecular Cell Biology*. Epub ahead of print 2021. DOI: 10.1038/s41580-
330 021-00418-x.
331 3. **Mercer J, Schelhaas M, Helenius A**. Virus entry by endocytosis. *Annual Review of*
332 *Biochemistry*;79. Epub ahead of print 2010. DOI: 10.1146/annurev-biochem-060208-
333 104626.
334 4. **Bayati A, Kumar R, Francis V, McPherson PS**. SARS-CoV-2 infects cells after viral
335 entry via clathrin-mediated endocytosis. *Journal of Biological Chemistry*;296. Epub ahead
336 of print 2021. DOI: 10.1016/j.jbc.2021.100306.

337 5. **Acker T van, Tavernier J, Peelman F**. The small GTPase Arf6: An overview of its
338 mechanisms of action and of its role in host- pathogen interactions and innate immunity.
339 *Int J Mol Sci*;20. Epub ahead of print 2019. DOI: 10.3390/ijms20092209.
340 6. **Gordon DE, Jang GM, Bouhaddou M, Xu J, Obernier K, *et al.*** A SARS-CoV-2
341 protein interaction map reveals targets for drug repurposing. *Nature*;583. Epub ahead of
342 print 2020. DOI: 10.1038/s41586-020-2286-9.
343 7. **Chen F, Shi Q, Pei F, Vogt A, Porritt RA, *et al.*** A systems-level study reveals host-
344 targeted repurposable drugs against SARS-CoV-2 infection. *Mol Syst Biol*;17. Epub ahead
345 of print 2021. DOI: 10.15252/msb.202110239.
346 8. **Harder JL, Menon R, Otto EA, Zhou J, Eddy S, *et al.*** Organoid single cell profiling
347 identifies a transcriptional signature of glomerular disease. *JCI Insight*;4. Epub ahead of
348 print 2019. DOI: 10.1172/jci.insight.122697.
349 9. **Mirabelli C, Wotring JW, Zhang CJ, McCarty SM, Fursmidt R, *et al.*** Morphological
350 cell profiling of SARS-CoV-2 infection identifies drug repurposing candidates for
351 COVID-19. *Proc Natl Acad Sci U S A*;118. Epub ahead of print 2021. DOI:
352 10.1073/pnas.2105815118.
353 10. **Sanjana NE, Shalem O, Zhang F**. Improved vectors and genome-wide libraries for
354 CRISPR screening. *Nature Methods*;11. Epub ahead of print 2014. DOI:
355 10.1038/nmeth.3047.
356 11. **Emmer BT, Sherman EJ, Lascuna PJ, Graham SE, Willer CJ, *et al.*** Genome-scale
357 CRISPR screening for modifiers of cellular LDL uptake. *PLoS Genet*;17. Epub ahead of
358 print 2021. DOI: 10.1371/JOURNAL.PGEN.1009285.

359 12. **Macia E, Ehrlich M, Massol R, Boucrot E, Brunner C, *et al.*** Dynasore, a Cell-
360 Permeable Inhibitor of Dynamin. *Dev Cell*;10. Epub ahead of print 2006. DOI:
361 10.1016/j.devcel.2006.04.002.
362 13. **Sviridov D, Miller YI, Ballout RA, Remaley AT, Bukrinsky M**. Targeting Lipid
363 Rafts—A Potential Therapy for COVID-19. *Front Immunol*;11. Epub ahead of print 2020.
364 DOI: 10.3389/fimmu.2020.574508.
365 14. **Li X, Zhu W, Fan M, Zhang J, Peng Y, *et al.*** Dependence of SARS-CoV-2 infection on
366 cholesterol-rich lipid raft and endosomal acidification. *Comput Struct Biotechnol J*;19.
367 Epub ahead of print 2021. DOI: 10.1016/j.csbj.2021.04.001.
368 15. **Mayor S, Parton RG, Donaldson JG**. Clathrin-independent pathways of endocytosis.
369 *Cold Spring Harb Perspect Biol*;6. Epub ahead of print 2014. DOI:
370 10.1101/cshperspect.a016758.
371 16. **Shang J, Wan Y, Luo C, Ye G, Geng Q, *et al.*** Cell entry mechanisms of SARS-CoV-2.
372 *Proc Natl Acad Sci U S A*;117. Epub ahead of print 2020. DOI:
373 10.1073/pnas.2003138117.
374 17. **Pia L, Rowland-Jones S**. Omicron entry route. *Nat Rev Immunol*. Epub ahead of print 26
375 January 2022. DOI: 10.1038/s41577-022-00681-9.
376 18. **Kim Y, Jang G, Lee D, Kim N, Seon JW, *et al.*** Trypsin enhances SARS-CoV-2
377 infection by facilitating viral entry. *Arch Virol*;167. Epub ahead of print 2022. DOI:
378 10.1007/s00705-021-05343-0.
379 19. **Wang H, Yang P, Liu K, Guo F, Zhang Y, *et al.*** SARS coronavirus entry into host cells
380 through a novel clathrin- and caveolae-independent endocytic pathway. *Cell Res*;18. Epub
381 ahead of print 2008. DOI: 10.1038/cr.2008.15.

382 20. **Zhou YQ, Wang K, Wang XY, Cui HY, Zhao Y, *et al.*** SARS-CoV-2 pseudovirus
383 enters the host cells through spike protein-CD147 in an Arf6-dependent manner. *Emerg*
384 *Microbes Infect*;11. Epub ahead of print 2022. DOI: 10.1080/22221751.2022.2059403.
385 21. **Koch J, Uckeley ZM, Doldan P, Stanifer M, Boulant S, *et al.*** TMPRSS2 expression
386 dictates the entry route used by SARS-CoV-2 to infect host cells. *EMBO J*;40. Epub ahead
387 of print 2021. DOI: 10.15252/embj.2021107821.
388
389

390 **Figure legends**

391 **Figure 1:** Huh-7 cells are resistant to the antiviral effect of camostat mesylate. A-B) Dose-
392 response curves of camostat mesylate (A) and the cathepsin B inhibitor Z-FA-FMK (B). Huh-7
393 cells were pre-treated with compound and infected with SARS-CoV-2 at MOI of 1 for 1h at
394 37°C. 48 hpi cells were fixed and permeabilized and stained with anti-N antibody. Cells were
395 imaged with high content imaging platform CX5 and analyzed with Cell profiler for image
396 segmentation. The % of infected cells were normalized to the non-treated infected condition.
397 Graph represents average SD of N=3 independent experiments with n=3 technical replicate,
398 each. C) Representative images of Huh-7 cells infected with SARS-CoV-2 or infected/treated
399 with camostat (500 nM) and Z-FA-FMK (500 nM). N protein staining is represented in magenta,
400 nuclei are in blue.

401

402 **Figure 2:** Screening of inhibitors of the dynamin-dependent entry pathways in Huh-7 cells. Huh-
403 7 cells were pre-treated with compounds at the indicated concentration and infected with SARS-
404 CoV-2 at MOI of 1 for 1 h at 37ºC. 24 hpi cells were fixed, permeabilized and stained with anti-
405 N antibody. Cells were imaged with high content imaging platform CX5 and analyzed with Cell
406 profiler for image segmentation.

407

408 **Figure 3:** Genetic depletion of ARF6 does not affect viral titers but reduce the percentage of
409 infected cells A-B) Viral titer determination of SARS-CoV-2-infected NTg, ACE2-KO ARF6-
410 KO Huh7 clones (MOI of 1) by $TCID_{50}$/ml at 24 and 48 hpi (A) and by RT-qPCR at 24dpi (B).
411 ACE2-KO was used as a negative control of infection. Viral infectious titer was determined by
412 $TCID_{50}$ on Vero E6 cells. Dashed line represents the limit of detection of the $TCID_{50}$ assay. C)

413 Representative images of SARS-CoV-2-infected NTg and KO-Huh7 clones (MOI of 10). N
414 protein staining is represented in magenta, nuclei are in blue (DAPI). The graph represents the
415 quantification of SARS-CoV-2 infected cells (MOI of 10) at 24 hpi. Cells were imaged with high
416 content imaging platform CX5 and analyzed with Cell profiler for image segmentation. The % of
417 infected cells was normalized to the non-treated infected condition. Graph represents average SD
418 of N=3 independent experiments with n=3 technical replicate, each.
419
420 **Figure 4.** ARF6 is important during SARS-CoV-2 internalization in Huh-7 cells. A) NAV-2729,
421 an ARF6 inhibitor was used to pre-treat Huh-7 cells in a 384-well plate 2 hrs prior infection with
422 SARS-CoV-2 (MOI of 1). Cells were harvested 48 hpi and subjected to the imaging pipeline for
423 viral quantification. 1:2 dose response curves were performed in triplicate with 3 technical
424 replicates, each. B) NTg Huh-7 were pre-treated with NAV-2927 (10 μM) and ARF6 KO were
425 pre-treated with dynasore (10 μM) for 2 h before infection with SARS-CoV-2 (MOI of 1). Virus
426 inoculum was removed 1 hpi and cells were incubated with fresh medium +/- compounds. Cells
427 were harvested 24 hpi and viral titer was determined by $TCID_{50}$. C-D) NAV-2729 was used to
428 pre-treat Huh7 cells 2 hrs prior infection with SARS-CoV-2 (MOI of 10) on ice. NTg and ARF6-
429 KO Huh7 cells were used as a control. 1 h post infection on ice, cells were washed twice and one
430 set was harvested in TRI reagent. The second set was incubated at 37´C to allow viral
431 internalization. One hour post incubation, cells were treated with trypsin to remove bound, non-
432 internalized virus and were harvested in TRI reagent. Bound and internalized virus were
433 determined by RT-qPCR: Graph in panel C shows % of bound virus over untreated control (NTg
434 Huh-7), whereas graph in panel D measures the internalized fraction of SARS-CoV-2 over the

435 bound fraction. Statistical t-test was performed on GraphPad Prism on N= 3 biological replicate
436 with at least 2 technical replicates, each. **p-value ≤0.01, **** p-value ≤0.001
437
438 **Figure 5.** ARF6 is critical for SARS-CoV-2 infection in more physiologic relevant cell types. A)
439 Human kidney organoids were collected and resuspended in maintenance media. Groups of four
440 organoids were infected with SARS-CoV-2 at MOI of 1. Organoids were washed twice and put
441 in culture on a matrigel-coated plate for 48 hrs. Cells were then harvested, and virus was
442 quantified by $TCID_{50.}$ Each dot represents a technical replicate of N=2 biologically independent
443 experiments. B) Calu-3 cells and Calu-3 transduced with a non-targeting guide (NTg) or ARF6-
444 targeting guide (ARF6) were seeded in 48-well plate and allowed to reach 80% confluence.
445 SARS-CoV-2 WA1 was used to infect cells at MOI of 1 for 24 hrs. Cells were then harvested,
446 and virus was quantified by $TCID_{50}$. Each dot represents a technical replicate. C) Representative
447 images (left) and quantification (right) of Calu3 transduced with a non-targeting guide (NTg) or
448 ARF6-targeting guide (ARF6) and infected with trypsin activated SARS-CoV-2 WA1 or SARS-
449 CoV-2 Omicron (MOI of 1) for 24 hrs. Cells were fixed, permeabilized and stained with anti-N
450 primary antibody and anti-mouse AF647 secondary antibody (N protein, magenta) and Hoechst
451 (nuclei, blue). Cells were imaged with the high content imaging platform CX5 and analyzed with
452 Cell profiler for image segmentation. Each dot represents the average of % of infected cells over
453 20 fields of image per well. Each dot represents a technical replicate.
454
455

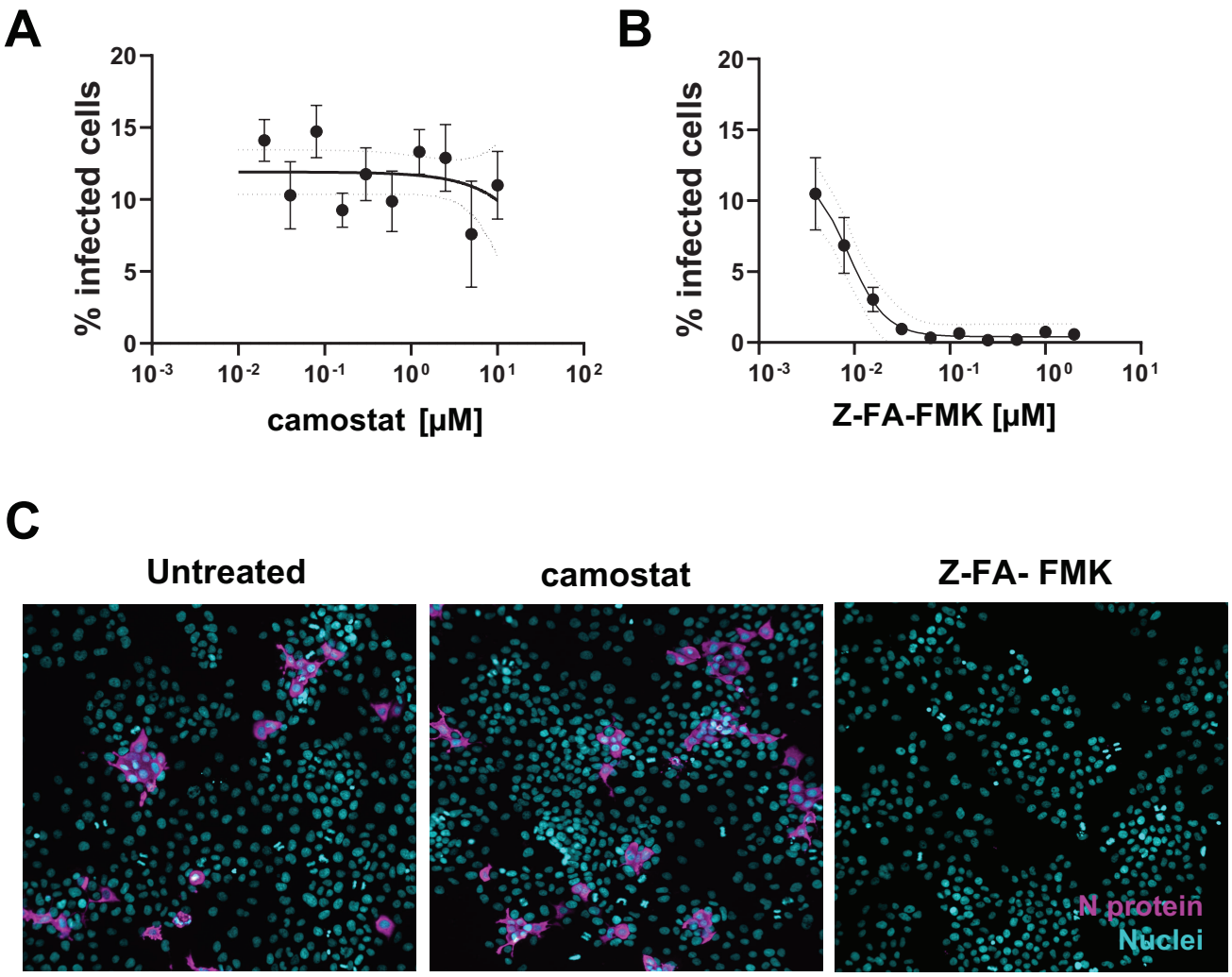
A
% infected cells
20
15
10
5
0
10-3
10-2
10-1
100
101
102
camostat [μM]
B
% infected cells
20
15
10
5
0
10-3
10-2
10-1
100
101
Z-FA-FMK [μM]
C
Untreated
camostat
Z-FA- FMK
N protein
Nuclei

Figure 1

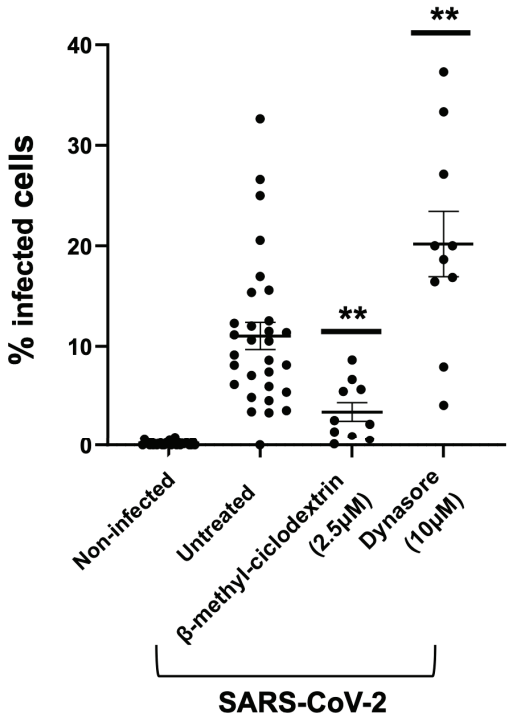
**
**
40
30
20
10
0
% infected cells
Non-infected
Untreated
β-methyl-ciclodextrin (2.5μM)
Dynasore (10μM)
SARS-CoV-2

Figure 2

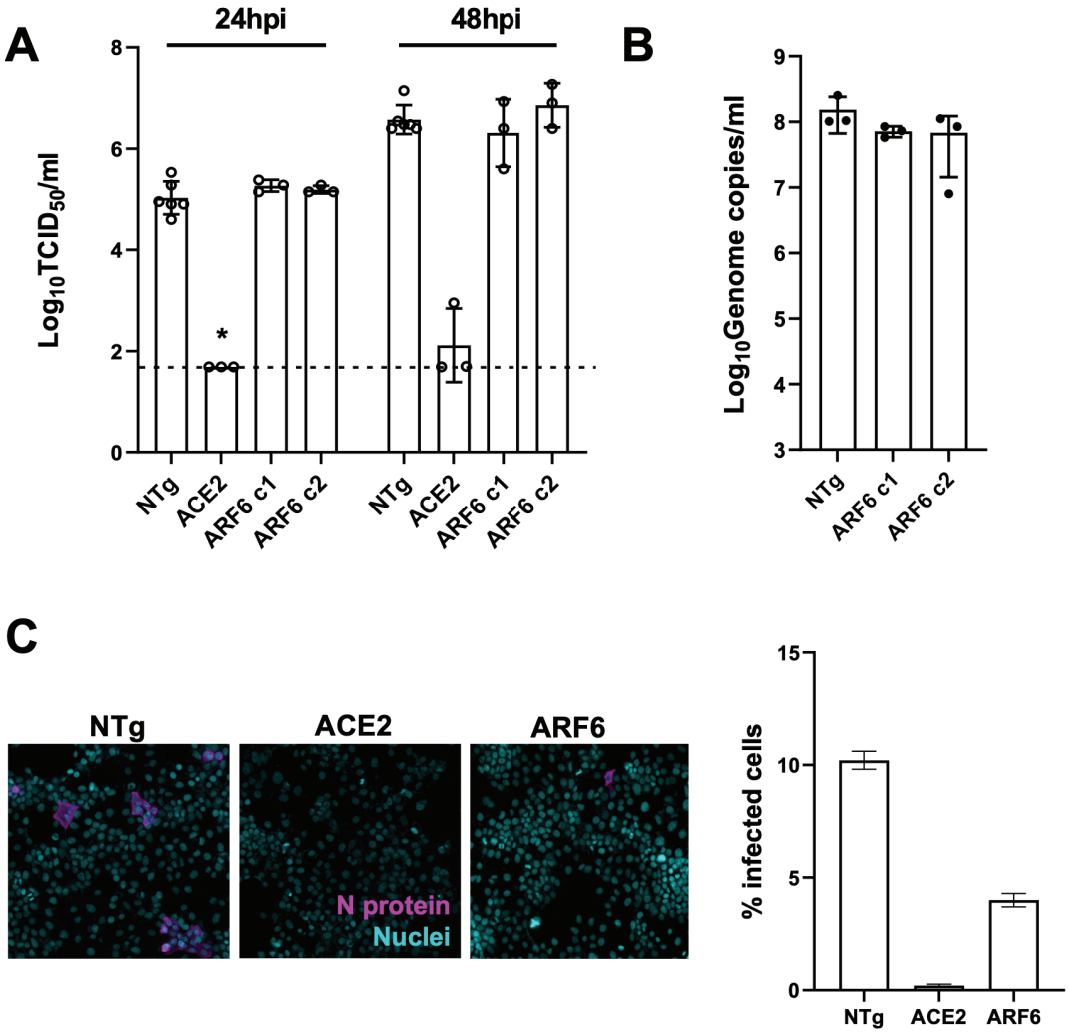
A
24hpi
48hpi
Log10TCID50/ml
8
6
4
2
0
*
NTg
ACE2
ARF6 c1
ARF6 c2
NTg
ACE2
ARF6 c1
ARF6 c2
B
Log10Genome copies/ml
9
8
7
6
5
4
3
NTg
ARF6 c1
ARF6 c2
C
NTg
ACE2
ARF6
N protein
Nuclei
% infected cells
15
10
5
0
NTg
ACE2
ARF6

Figure 3

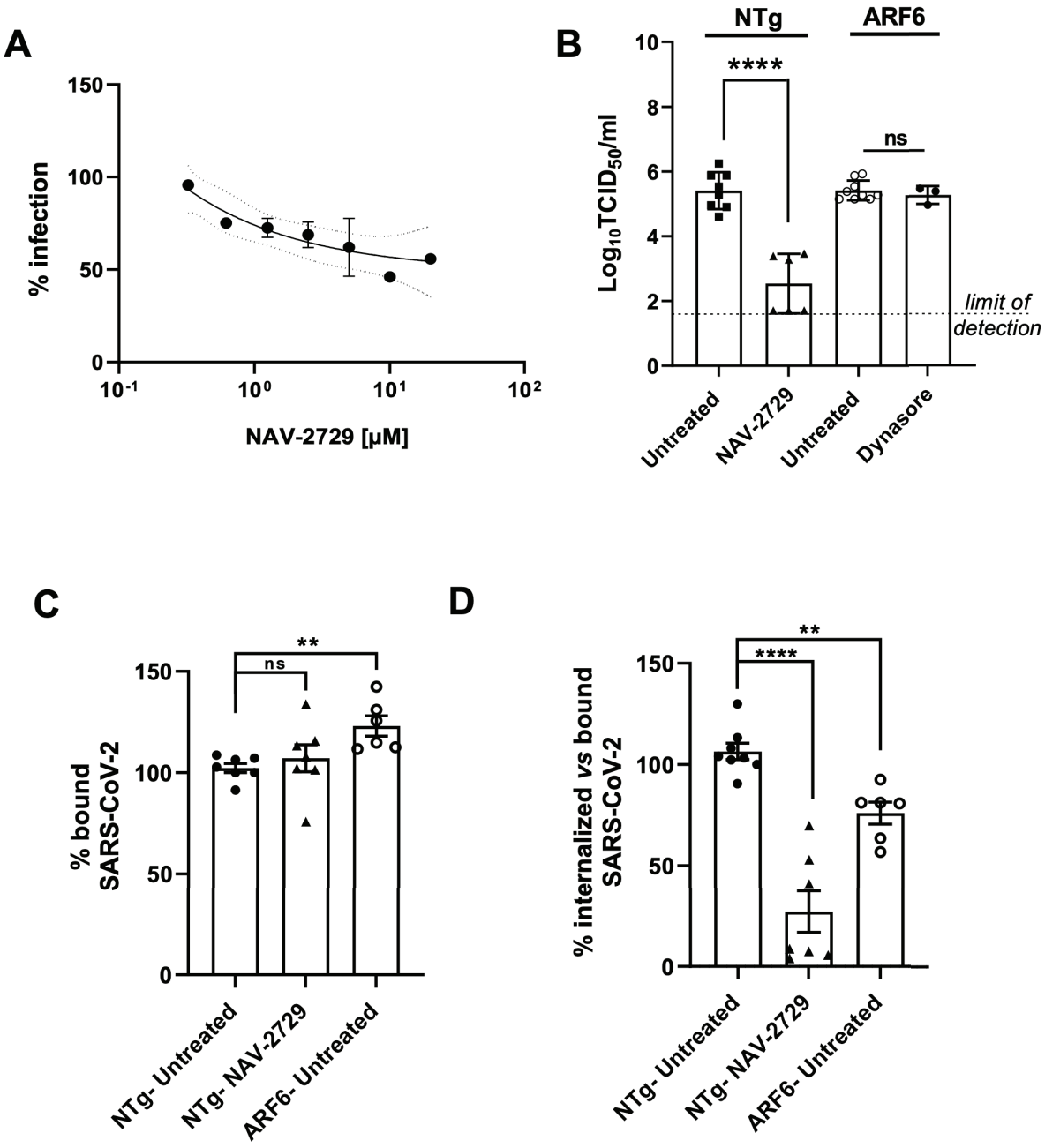
A
% infection
150
100
50
0
10^{-1}
10^{0}
10^{1}
10^{2}
NAV-2729 [µM]
B
NTg
ARF6
****
ns
$Log_{10}TCID_{50}$/ml
10
8
6
4
2
0
limit of detection
Untreated
NAV-2729
Untreated
Dynasore
C
**
ns
% bound SARS-CoV-2
150
100
50
0
NTg- Untreated
NTg- NAV-2729
ARF6- Untreated
D
**
****
% internalized vs bound SARS-CoV-2
150
100
50
0
NTg- Untreated
NTg- NAV-2729
ARF6- Untreated

Figure 4

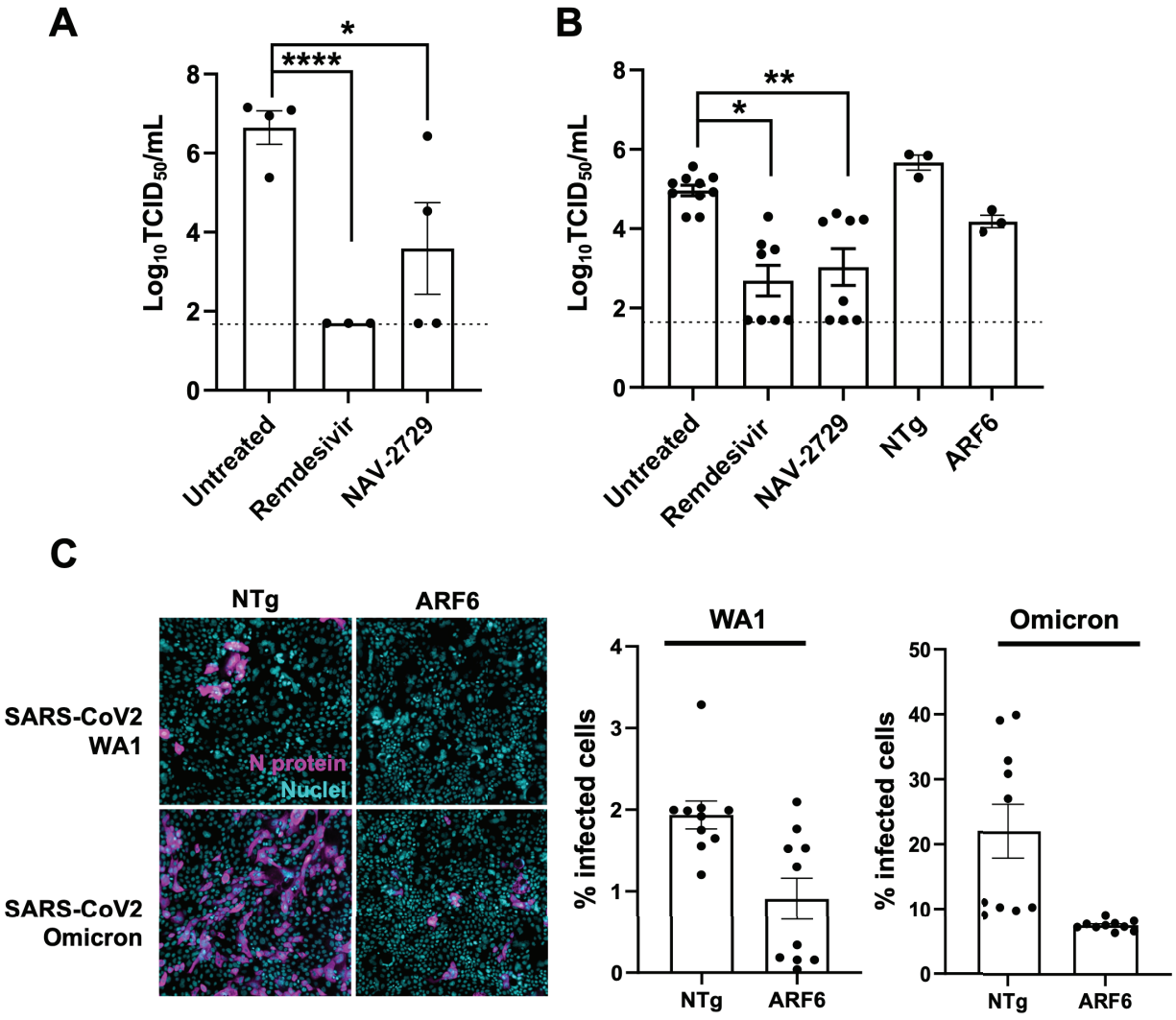
A
B
C
Log10TCID50/mL
Untreated
Remdesivir
NAV-2729
NTg
ARF6
SARS-CoV2 WA1
SARS-CoV2 Omicron
N protein
Nuclei
WA1
Omicron
% infected cells

Figure 5

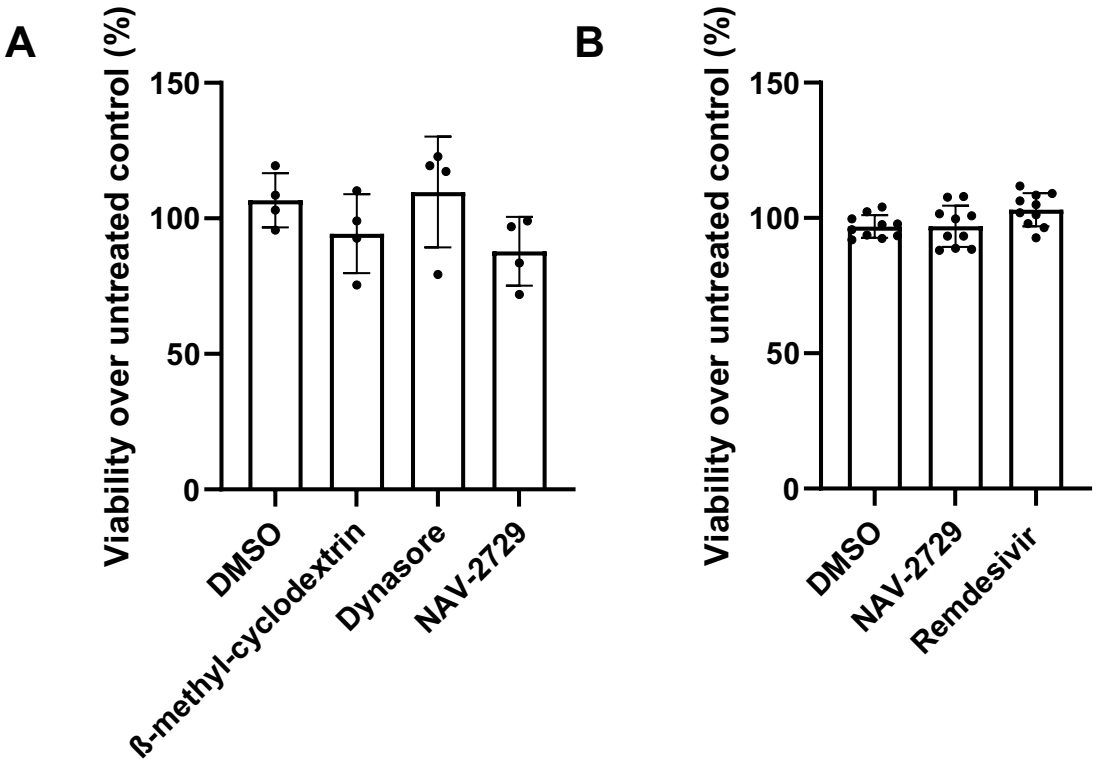

Supplementary figure 1: A-B) Toxicity assay of selected drugs by Resazurin assay in Huh-7 (panel A) and Calu-3 cells (panel B).

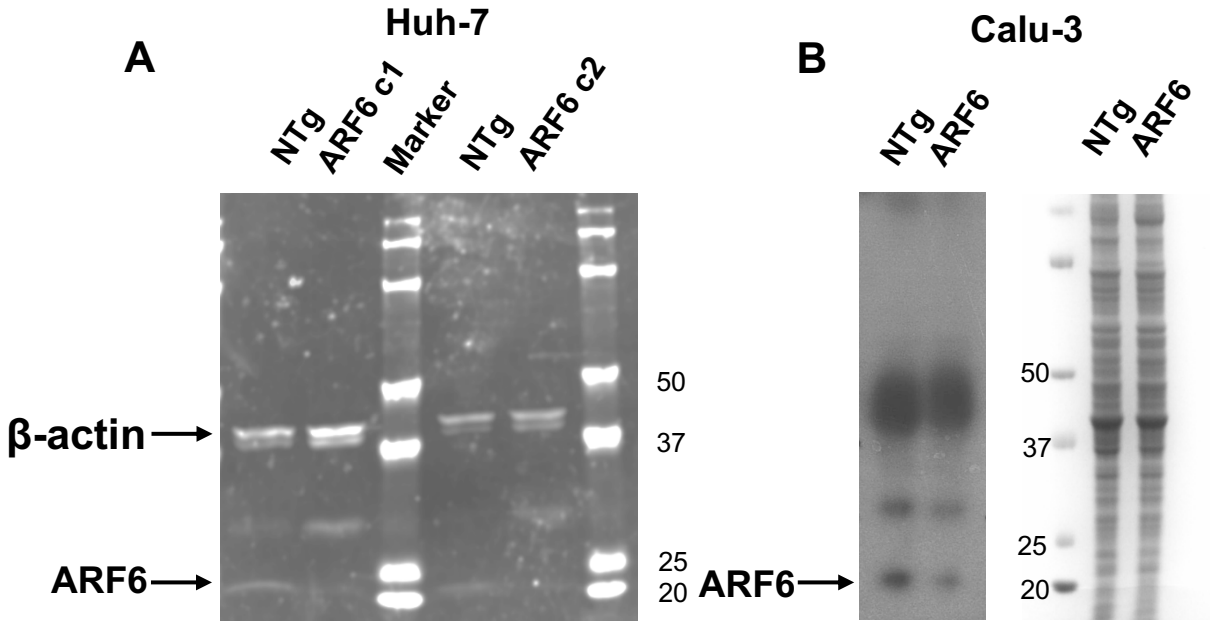

Supplementary figure 2: Western blot for ARF6 expression. A) Huh-7 lysates from non-targeting (NTg) and 2 clones of ARF6-knock-out (KO) preparations were obtained from cells seeded overnight in a 6-well plate and analyzed for ARF6 expression by Western blot. ß-actin was used as a loading control. Molecular weight marker (in kDa) is shown on the right. B) NTg and ARF6-KO Calu-3 cells were similarly obtained and analyzed by Western blot. As a loading control, a Coomassie blue staining of the gel was performed. Molecular weight marker (in kDa) is shown in the middle.

Supplementary Table 1: Sequences of sgRNAs for targeted CRISPR/Cas9 knockout.

Target gene(s)	gRNA	sgRNA
ARF6	1	CCTGGCGAGCCTCATCGATG
ARF6	2	CATTACTACACTGGGACCCA
ACE2	1	GTTCATTTCCAAGTCCGCTG
Nontargeting	1	TACCAAGCAAATGAGCAGGG

Supplementary Methods

Western blot. Cells were lysed in RIPA buffer (Pierce, 89900) with PhosSTOP (Roche, 04906845001) and cOmplete EDTA-free protease inhibitor cocktail (Roche, 11873580001) on ice. After vortexing to ensure a complete lysis, cells were centrifuged at 4°C, 14,000 × g for 15 min. The supernatant was mixed with β-mercaptoethanol-containing (10%) Laemmli buffer (Bio-Rad, cat nr. 1610747) at 3:1 ratio and denatured at 90°C for 10 min with a heat block. Samples were spun down before being loaded in a 4 to 20% Mini-Protean TGX gels (Bio-Rad, number 456-1096). Gels were run at 80 to 100 V for 45 min to 1 h and transferred to Immobilon-FL transfer membranes (IPFL00010) using semidry transfer at 10 V for 45 min. Membranes were blocked in 5% bovine serum albumin fat-free milk prepared in PBS containing 0.05% Tween 20 for a minimum of 2 hrs at room temperature. Membranes were incubated with primary antibodies (anti-ARF6 antibody (3A-1), Santa Cruz, cat nr. sc-7971 and anti-β–actin, 8H10D10, Cell Signaling, cat nr. 3700S) at 4°C by rocking overnight. Antibodies were washed off the membranes with four 15-min rocking periods using fresh changes of PBS. Secondary antibody incubation was done using fluorescent LI-COR antibodies (anti-rabbit IgG, cat. nr. 926-68071; and anti-mouse IgG, cat nr. 926-32210) or regular secondary antibody (anti-mouse IgG HRP, Thermo Fisher, A9044) diluted 1:10,000 in PBS for 1 hr at room temperature with gentle rocking. Membranes were washed with PBS as before and visualized using a LI-COR Odyssey Imager (Huh7 cells) or a regular imager after development with the Pierce™ ECL Plus Western Blotting Substrate (Thermo Fisher, cat nr. 32132X3) (Calu-3 cells).

Viability assay. Huh-7 cells or Calu-3 were seeded in a 96-well plate at 10,000 cells/well and allowed to adhere overnight. The next day, medium was replaced by medium with compounds or vehicle (DMSO, at the highest concentration used) and resazurin (Biotium, 30025-1) was added according to the manufacturer´s instruction. One day post treatment (to mimic infection condition), absorbance (590 nm) was measured with a Synergy™ HTX plate reader.